Yu She[1,2]
Department of Mechanical and Aerospace Engineering,
Ohio State University,
Columbus, OH 43210
e-mail: she.22@osu.edu

Zhaoyuan Gu[3]
Department of Mechanical and Aerospace Engineering,
Ohio State University,
Columbus, OH 43210
e-mail: zgu78@gatech.edu

Siyang Song
Walker Department of Mechanical Engineering,
University of Texas at Austin,
Austin, TX 78712
e-mail: sysong@utexas.edu

Hai-Jun Su
Professor
Fellow ASME
Department of Mechanical and Aerospace Engineering,
Ohio State University,
Columbus, OH 43210
e-mail: su.298@osu.edu

Junmin Wang
Professor
Fellow ASME
Walker Department of Mechanical Engineering,
University of Texas at Austin,
Austin, TX 78712
e-mail: JWang@austin.utexas.edu

Design, Modeling, and Manufacturing of a Variable Lateral Stiffness Arm Via Shape Morphing Mechanisms

In this article, we present a continuously tunable stiffness arm for safe physical human–robot interactions. Compliant joints and compliant links are two typical solutions to address safety issues for physical human–robot interactions via introducing mechanical compliance to robotic systems. While extensive studies explore variable stiffness joints/actuators, variable stiffness links for safe physical human–robot interactions are much less studied. This article details the design and modeling of a compliant robotic arm whose stiffness can be continuously tuned via cable-driven mechanisms actuated by a single servo motor. Specifically, a 3D-printed compliant robotic arm is prototyped and tested by static experiments, and an analytical model of the variable stiffness arm is derived and validated by testing. The results show that the lateral stiffness of the robot arm can achieve a variety of 221.26% given a morphing angle of 90 deg. The variable stiffness arm design developed in this study could be a promising approach to address safety concerns for safe physical human–robot interactions. [DOI: 10.1115/1.4050379]

Keywords: cable-driven mechanisms, compliant mechanisms, mechanism design, robot design, variable stiffness

1 Introduction

As robots become increasingly integrated with humans in various domains [1], safety becomes an essential consideration in physical human–robot interactions. To increase the safety for physical human–robot interaction, researchers have introduced mechanical compliance to robots, either in their joints or links. Extensive research has been conducted on joint compliance, while limited studies have explored link compliance.

A typical example of joint compliance is the anthropomorphic hand system [2–4], where superimposed cam mechanisms and floating springs are employed at the joint, such that kinetic energy from an impact could be absorbed and stored to the springs. Other classic joint compliance designs include the variable impedance actuation (VIA) and variable stiffness actuators (VSAs) [5–8]. Their joint stiffness is able to change rapidly and continuously to satisfy the safety requirements. The previous studies have researched more on the VSA [9–12].

Compared with joint compliance, link compliance is much less explored [13,14]. Researchers developed switch compliant links to ensure safety [15–17]. The basic idea is that the robot link is rigid for normal operation but could switch to a compliant mode given an external force exceeding a threshold. An inherently safe robotic arm is developed in Refs. [18,19] via optimization of the beam profile. Unlike the VSA, in which joint stiffness is continuously adjustable, all of these switch designs do not offer continuously controllable stiffness.

To address the safety concerns of physical human–robot interactions, the variable stiffness links (VSLs) lately have drawn increasing attention from researchers. Stilli et al. [20] investigated a soft manipulator with controllable stiffness via combining pneumatic and tendon-driven actuators. They also developed a VSL with a plastic meshed silicone wall and an airtight chamber [21]. The stiffness of the manipulator can be tuned by regulating the air pressure in the silicone chamber. On top of the pneumatic-controlled VSL manipulator, they recently studied open-loop position controls with the VSL robot and demonstrated that the VSL robot outperforms a manipulator with 3D-printed rigid links [22]. She et al. [23–25] proposed a novel VSL, which builds upon a compliant parallel-guiding mechanism. The mechanism leverage a set of four-bar linkages to control the shape of the link, yielding a tunable stiffness robotic link. Zeng et al. [26] designed a novel VSL through pneumatic actuated layer jamming methods. The VSL also builds upon a compliant parallel-guiding mechanism, which includes two flexible beams sandwiched with thin plastic friction layers. The stiffness of the mechanisms can be tuned by controlling the air pressure applied to the friction layers. Similar layer jamming structures are explored to develop compliant robotic gripper with variable stiffness [27].

Modeling compliant links is more complex than modeling compliant joints since it contains infinite degrees-of-freedom (DOFs).

[1]Corresponding author.
[2]Present address: Computer Science and Artificial Intelligence Laboratory, Massachusetts Institute of Technology, Cambridge, MA 02139.
[3]Present address: George W. Woodruff School of Mechanical Engineering, Georgia Institute of Technology, Atlanta, GA 30332.

Paper presented at the 2020 ASME IDETC (Paper No. DETC2020-22035).
Contributed by the Mechanisms and Robotics Committee of ASME for publication in the Journal of Mechanisms and Robotics. Manuscript received September 28, 2020; final manuscript received January 30, 2021; published online March 26, 2021. Assoc. Editor: Pinhas Ben-Tzvi.

Topological synthesis [28], beam theory [29,30], screw theory based methods [31–33], and pseudo-rigid-body (PRB) model [34,35] are common methods for modeling the compliant mechanisms. Among those approaches, the PRB model offers a simplified and computationally efficient solution to model the compliant mechanisms. This method is particularly helpful in the initial design stage, which will be used and discussed in this article.

In this article, we propose a novel compliant robotic arm for physical human–robot interaction. The stiffness of the arm can be continuously tuned by morphing the shape of the arm, i.e., changing the second moment of inertia of the cross section via a set of cable-driven mechanisms.

We start this article with the motivation for this research in Sec. 2. The mechanical design of the morphing arm and the associated cable-driven mechanism is presented in Sec. 3. In Sec. 4, kineto-static (kinematic and static) analysis of the cable-driven mechanisms and the variable stiffness modeling of the shape morphing arm are derived. A 3D-printed prototype and extensive experiments are presented in Sec. 5, followed by discussions in Sec. 6. Finally, conclusions are addressed in Sec. 7.

2 Motivations

In a typical rest-to-rest task, a robot generally performs as follows: (1) it increases its speed from 0 during the first stage, (2) it reaches and maintains a stable maximum speed in the second stage to maximize the time efficiency, and (3) it gradually reduces its speed to 0 and finally reaches the destination at the end of the third stage.

A high operation speed of the manipulator is desired from the perspective of time efficiency, and high safety is required for physical human–robot interactions. Here, we use impact force [14] as a safety criterion to evaluate the severity of the potential impact result. The impact force is determined by impact velocity, robot stiffness, and mass involved in the impact (including robot effective mass and object effective mass) [36]. Given a particular manipulation task, the mass of the objects is generally fixed, and we do not have control over it. Here, we consider the effect of the impact velocity $v(t)$ and robot stiffness $k(t)$ on the impact force $F(t)$.

Let us first consider a traditional robot manipulator with constant stiffness. Fast motion of the manipulator permits time efficiency but may cause a severe injury, while slow motion may admit high safety but can be time consuming. High performance (e.g., time efficiency) and high safety are challenging to achieve simultaneously for traditional robots with constant stiffness. However, this can be done by applying the concept of variable stiffness robotic arms.

Now let us consider a robotic arm whose stiffness can be actively regulated. One can tune down the robot stiffness during fast motion, such that the robot is time efficient, while keeping high safety. Similarly, when the robot runs slow for position control or force control, one can tune up the robot stiffness to increase its accuracy and resolution. In this way, the variable stiffness arm provides a potential solution to simultaneously achieve high safety and high performance (e.g., time efficiency, high accuracy, and high resolution). A schematic view of robot operation velocity $v(t)$, the robot stiffness $k(t)$, and the potential impact force $F(t)$ are shown in Fig. 1. The robotic arm can be tuned with low stiffness given fast motion to ensure inherent safety, while it is tuned with high stiffness given slow motion for high performance (e.g., to achieve accurate position control or force control).

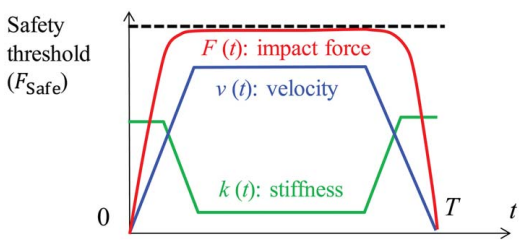

Fig. 1 A schematic view of the functioning principle of the concept of the variable stiffness arm for a typical rest-to-rest task

Therefore, there is a need to develop robotic arms with variable stiffness since they potentially address the two competing criteria: high performance and high safety. There are a few methods to achieve the stiffness variation of the robot arm, such as tuning the second moment of inertia, controlling effective length, and changing material modulus. In this study, we studied the shape morphing solution, i.e., changing the second moment of inertia to obtain the tunable stiffness via cable-driven mechanisms.

3 The Mechanical Design

This section details the mechanical design of the shape morphing arm and the associated cable-driven mechanisms.

3.1 Design Logic Overview. In this section, we briefly go through the logic behind the development of the variable stiffness link. Inspired by the rotating Euler beam [37], we are interested in designing a variable stiffness link by regulating the second moment of inertia. In particular, we focus on the compliant parallel-guiding mechanism [38] that is composed of two flexible beams.

One potential solution to regulate the second moment of inertia of the beam is to morph the shape of the flexible beams (Sec. 3.2). Next, we need to design an actuation mechanism to achieve the shape morphing function. A solution that first came into mind is cable-driven mechanisms due to their lightweight (Sec. 3.3).

We want the shape morphing motion to be performed uniformly along the flexible beams. To achieve this goal, one may employ large sets of the cable-driven mechanism along with the beams. This will result in a more complicated design with heavyweight, which contradict our expectations. We end up employing three sets of the cable-driven mechanism as a tradeoff between the uniform shape morphing and the simple/light design (Sec. 3.3).

In addition, we want to minimize the number of actuators to reduce the weight of the variable stiffness link. Therefore, we designed a universal transmission shaft to transmit the motion from the actuator to the three sets of the cable-driven mechanism. We end up applying a single motor to achieve the shape morphing function (Sec. 3.3).

Furthermore, it is expected that the two flexible beams perform symmetric deformations to keep the link stable and robust. Therefore, we designed the winding patterns of the cable loops to achieve the goal (Sec. 3.4).

Finally, to maximize the energy efficiency of the motor, we designed the bending control pulleys, which transfer most of the motor torque to the lateral force to bend the flexible beams (Sec. 3.4). Instead of relying on the strain energy of the flexible beams for the recovery process (i.e., from the morphed configurations to the original configuration), we would like to have active control for the recovery process. We designed the recovering control pulley to accomplish the task (Sec. 3.4).

3.2 The Shape Morphing Concept. The conceptual design of the shape morphing arm is detailed in Fig. 2. Here, the shape morphing concept builds upon a compliant parallel-guiding mechanism, as shown in Fig. 2(*a*), top, which is a typical compliant mechanism with one DOF providing accurate linear motion capabilities [39]. The mechanism includes two flexible beams on its sides, which can be continuously turned between a flattened configuration and a curved configuration. The flattened configuration produces a small value of the second moment of inertia, resulting in a compliant mode of the mechanism. The mechanism laterally deforms, as shown in Fig. 2(*b*), top, if a lateral force is applied at the tip due to its high compliance. Figure 2(*c*) top shows the cross section of the parallel-guiding mechanism in the flattened configuration.

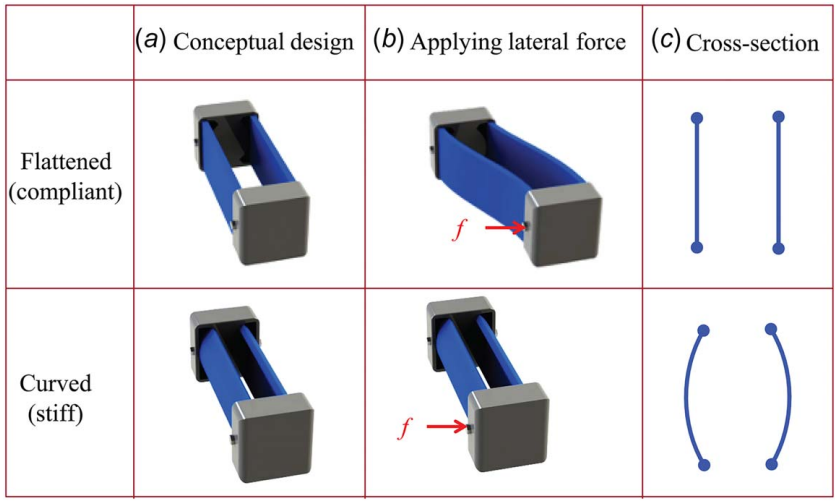

Fig. 2 The conceptual design of the shape morphing arm: (*a*) the shape morphing arm builds upon a compliant parallel-guiding mechanism, (*b*) the reaction of the arm given a lateral force at the tip, and (*c*) the cross section of the shape morphing arm

In this study, the flattened beams on both sides of the parallel-guiding mechanism can be tuned to a curved configuration, as shown in Fig. 2(*a*), bottom. The curved beams produce a large value of the second moment of inertia, yielding a relatively stiff mechanism. The mechanism remains still, as shown in Fig. 2(*b*), bottom, given a lateral force at its tip due to its high stiffness. Figure 2(*c*), bottom, shows the cross section of the mechanism under the curved configuration. By continuously tuning the flexible beams between the flattened and the curved configuration, one can achieve a variable stiffness link.

Now we have a solution, which is the shape morphing method, to achieve a variable stiffness robotic arm. The next question is how to design an actuation mechanism to realize the shape morphing approach. In what follows, we will present the development of a cable-driven system to do the task.

3.3 Mechanical Design of the Shape Morphing Arm. The shape morphing arm is composed of a servo motor, four pairs of bearing frame, two universal transmission shaft, a base house, an end house, an end load, two flexible beams, and three cable-driven mechanisms, as shown in Fig. 3. The key components are the flexible beams that are assembled on both sides of the morphing arm, which are the source of the variable lateral stiffness. The flexible beams are flattened in Fig. 3 under a compliant mode, and they can be morphed in curved shapes under stiff modes via cable-driven mechanisms. The variable stiffness is achieved by morphing the shape of the flexible beams.

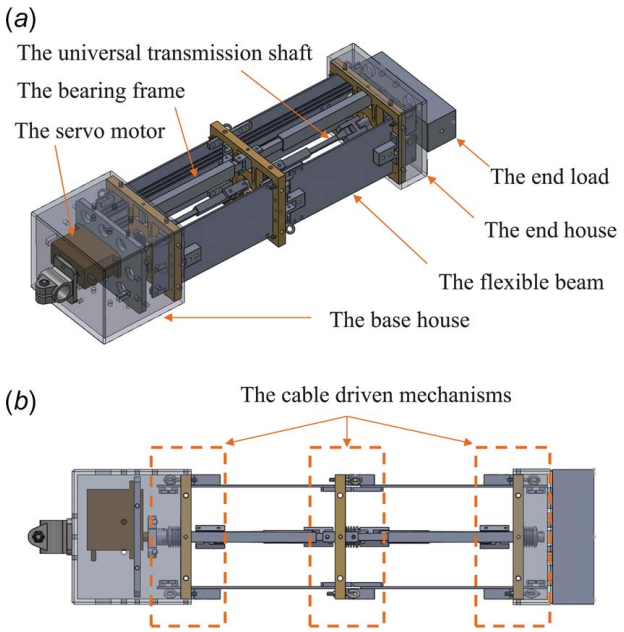

Fig. 3 The design of the proposed shape morphing arm: (*a*) the stereoscopic view of the arm and (*b*) the top view of the arm (Color version online.)

In addition to the variable lateral stiffness, we would like to maintain the high rigidity in the vertical direction for the purpose of carrying loads. Therefore, four bearing frames are designed to connect the cable-driven mechanisms. The left cable-driven mechanism is fixed on the base house, and the right cable-driven mechanism is attached to the end house. The bearing frames are designed as a square rail with linear guides permitting extension and contraction, and the connections between the bearing frames and cable-driven mechanisms are rotational joints in the lateral direction. As a result, the shape morphing arm behaves as a compliant parallel-guiding mechanism, while it remains rigid in the vertical direction given lateral forces.

A servo motor sitting in the base house provides torque to morph the flexible beams via cable-driven mechanisms. To morph the flexible beam uniformly, three cable-driven mechanisms are assembled and distributed along the morphing arm. To reduce the number of the actuators, two universal transmission shafts are designed to connect the three cable-driven mechanisms such that a single servo motor can actuate all cable-driven mechanisms simultaneously and further morph the flexible beam uniformly.

The central line of the flexible beams is assembled on the cable-driven mechanisms, while the up edge and bottom edge of the flexible beams are connected with cables for the morphing purpose. The base house, the end house, the cable-driven mechanisms, and the bearing frames basically form the "skeletons," while the flexible beams comprise the "muscles" of the shape morphing arm.

3.4 Detailed Design of the Cable-Driven Mechanism. The detailed design of the cable-driven mechanism is presented in this section. The three cable-driven mechanisms are identical, and the detailed design is shown in Fig. 4. The bold lines in gray color represent the flattened shape of the flexible beams under the compliant mode, while the bold lines in black color represent the curved shape of the beams under stiff mode. The centers of the flexible beams (D, D') are fixed to the cable-driven mechanism. The ends of the flexible beams (B_1, B_2) are tied with cables. The cables

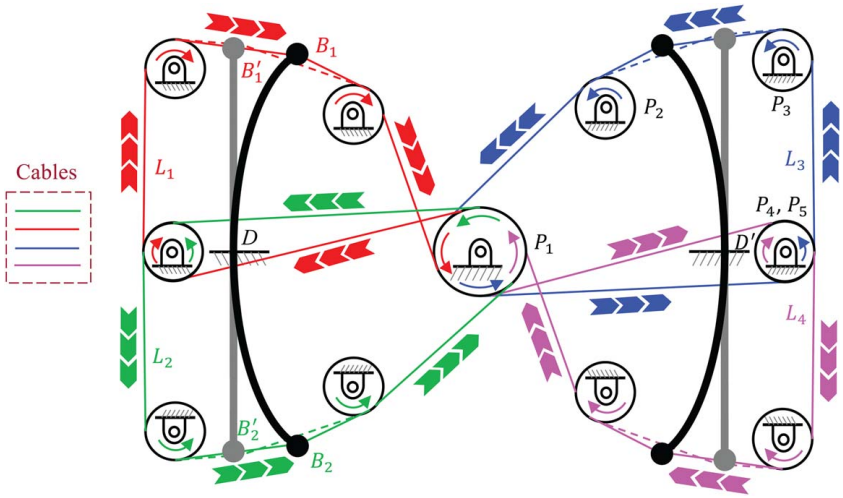

Fig. 4 The design of the cable-driven mechanism. The mechanism includes four cable loops (blue, red, green, magenta), and each loop contains four pulleys. The chevron arrows and the rotational arrows represent the motion direction of cables during the flexion process (from B_1B_2 to $B_1'B_2'$), while the extension process (from $B_1'B_2'$ to B_1B_2) has the opposite motion direction. (Color version online.)

pull the end of the beams, resulting in deformations of the flexible beams. There are four cable loops in each cable-driven mechanism, including L_1, L_2, L_3, and L_4, from which the diagonal loops share the same winding route, and the adjacent loops have slightly different windings around the center pulley. Each cable loop goes through four pulleys: the center pulley (P_1), bending control pulley (P_2), recovering control pulley (P_3), and the base pulley (P_4). The pulleys are placed symmetrically around the center, and the center pulley is fixed on the servo motor and shared by the four cable loops. Given a rotary motion from the center pulley, the four cable loops are actuated simultaneously, yielding the deformation of the two flexible beams symmetrically. The chevron arrows and the rotational arrows represent the motion direction of the cable loops and pulleys, respectively, during the flexion process (from B_1B_2 to $B_1'B_2'$). The extension process (from $B_1'B_2'$ to B_1B_2) has the opposite motion direction.

We take the loops of L_1 and L_2 as examples to illustrate how the cable-driven mechanism achieves the shape morphing via the servo motor. Starting from L_1 under the flattened shape, the cable is attached to and starts from the edge of the flexible beam B_1'. After winding through a few pulleys, the cable ends with and is attached to B_1' in a loop. By following the arrow directions, the route of L_1 (L_4) can be described as $B_1' \rightarrow$ bending control pulley $\rightarrow$ center pulley $\rightarrow$ base pulley $\rightarrow$ recovering control pulley $\rightarrow B_1'$. Similarity, the route of L_2 (L_3) can be described as $B_2' \rightarrow$ bending control pulley $\rightarrow$ center pulley $\rightarrow$ base pulley $\rightarrow$ recovering control pulley $\rightarrow B_2'$. Given a counterclockwise motor torque, the flexible beams are pulled from the flattened shape (B_1' and B_2') to the curved shape (B_1 and B_2), and vice versa. The four cable loops allow the shape morphing of the flexible beam symmetrically, and the three cable-driven mechanisms permit the shape morphing uniformly.

The bending control pulley and recovering control pulley are designed in this study to enhance the moment arm and further reduce the motor torque to actuate the bending or recovering motion of the flexible beams. These pulleys are placed at positions to have the cable perpendicular to (approximately) the flexible beams.

4 Modeling of the Morphing Arm

In this section, we study the kinematics of the cable-driven mechanism, the static models of the flexible beams, as well as the lateral stiffness models of the shape morphing arm.

4.1 Kinematics of the Cable-Driven Mechanism. Consider the cross-sectional plane of the flexible beam, the flexible beam is actually an initially straight pinned-pinned beam, which is fixed in the middle (point D in Fig. 4) via attaching on the cable-driven mechanisms and is deformed at the edges (point B_1' and B_2' in Fig. 4) by pulling the cables.

The PRB model is used here to model the kinematics of the flexible beams. Due to similarity, we only need to analyze one cable loop, e.g., the upper right loop L_3, as shown in Fig. 5(*a*), and its

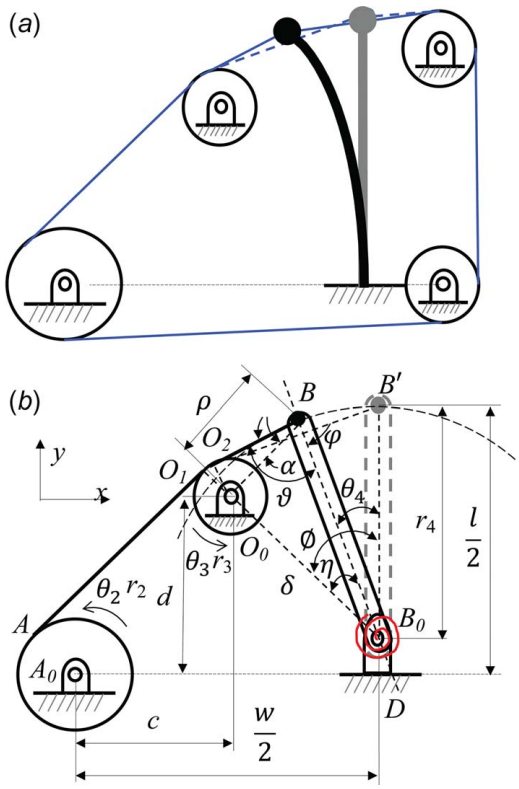

Fig. 5 (*a*) The cable loop with the flexible beam and (*b*) the cable loop with the PRB model

PRB model is shown in Fig. 5(*b*). Assume the flexible beam has a height, thickness, and length of l, t, and L, respectively. Assume the two flexible beams are spaced with a distance of w. If we use r_4 to represent the length of the PRB link, it can be calculated by

$$r_4 = \frac{\gamma l}{2} \tag{1}$$

where γ is the character radius factors. The stiffness of the torsional spring of the PRB model can be calculated as follows:

$$k_c = \frac{\gamma K_\theta E I_z}{l/2} \tag{2}$$

where K_θ is the stiffness constant of the PRB model and $I_z = Lt^3/12$. Note, $\gamma = 0.85$ and $K_\theta = 2.68$ considering the cable perpendicularly pulls the flexible beams [40].

Assume r_2 and r_3 represent the radius of the center pulley and the bending control pulley, and θ_2, θ_3, and θ_4 are rotation angles of the center pulley, the bending control pulley, and the PRB link, respectively. The motion of the pulleys satisfies the relation $\theta_2 r_2 = \theta_{3r3} \approx \theta_4 r_4$. Given the input angle θ_2 from the servo motor, the angle θ_4 can be calculated by

$$\theta_4 \approx \frac{r_2 \theta_2}{r_4} \tag{3}$$

We next specify the actuation torque of the servo motor with further kinematics analysis. The parameters are labeled as shown in Fig. 5(*b*). Let A_0 and O_0 represent the rotation center of the center pulley and the bending control pulley. B_0 is the rotation center of the PRB link r_4. The coordinates of A_0, O_0, and B_0 are (0, 0), (c, d), and (w/2, l/2 − r_4), respectively. The distance δ between O_0 and B_0 can be calculated as follows:

$$\delta = \sqrt{\left(\frac{w}{2} - c\right)^2 + \left(d - \frac{(1-\gamma)l}{2}\right)^2} \tag{4}$$

Assume B' represents the end position of the link r_2 under the flattened shape, and B represents its arbitrary morphed location. B' has a constant coordinate of (w/2, l/2). The angle ϕ between $O_0 B_0$ and $B'B_0$ is also a constant and can be calculated by

$$\phi = \arccos\left(\frac{d - \frac{(1-\gamma)l}{2}}{\delta}\right) \tag{5}$$

The angle η between $O_0 B_0$ and $B B_0$ can be expressed as follows:

$$\eta = \phi - \theta_4 \tag{6}$$

The distance ρ between point B and O_0 can be obtained by

$$\rho = \sqrt{\delta^2 + r_4^2 - 2\delta r_4 \cos\eta} \tag{7}$$

The angle φ between BO_0 and BB_0 can be calculated by

$$\varphi = \arccos\left(\frac{\rho^2 + r_4^2 - \delta^2}{2\rho r_4}\right) \tag{8}$$

Assuming O_1 and O_2 are the points of the tangency between the cable and the bending control pulley, the angle α between BO_2 and BO_0 is expressed as follows:

$$\alpha = \arcsin\left(\frac{r_3}{\rho}\right) \tag{9}$$

Then, we can calculate the force direction, i.e., the angle ϑ between BO_2 and the PRB link

$$\vartheta = \alpha + \varphi \tag{10}$$

Consider a single cable loop, the internal force F_c of the cable can be calculated as follows to overcome the stiffness of the torsional springs:

$$F_c = \frac{k_c \theta_4}{r_4 \sin\vartheta} \tag{11}$$

Finally, consider four similar cases with a single servo motor, the required torque can be stated as follows:

$$\tau = 4 F_c r_2 \tag{12}$$

The geometric parameters of the cable-driven mechanism and the morphing arm are provided in Table 1. Given the parameters in Table 1 with a counterclockwise angular input of the center pulley, the motion of the cable-driven mechanism is shown in Fig. 6.

4.2 Mechanics of the Flexible Beams. The PRB model provides a convenient way for kinematics analysis and torque identification. However, it cannot provide the exact shape of the flexible beams, which is required for calculating the variable stiffness. Therefore, we will derive the static model for the flexible beams under large deformations. Recall the flexible beam has a length, height, and thickness of L, l, and t, respectively. Assume the material of the beam is with Young's modulus of E. Given an actuation from the center pulley, the flexible beam may deform as shown in Fig. 7(*b*). The flexible beam is actually a pinned-pinned segment. If we consider half of the segment, it can be modeled with a cantilever beam, as shown in Fig. 7(*a*).

Given external forces of F_x and F_y and an external moment of M_0 at the tip of the cantilever beam, it has a tip deformation of (a, b) and tip deformation angle of Ψ. The moment along the beam in an arbitrary point $P(x, y)$ can be expressed as follows:

$$M(x, y) = F_x(b + y) - F_y(a - x) - M_0 \tag{13}$$

Table 1 Geometric parameters of the cable-driven mechanism and the morphing arm

Parameters	Value (mm)	Parameters	Value (mm)
L	400	l	70
t	2	w	95
c	16	d	30
r_2	8	r_3	1

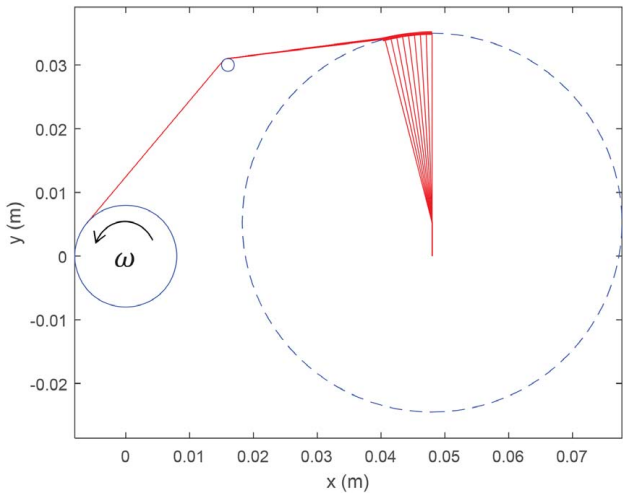

Fig. 6 The kinematics simulation of the cable-driven mechanism

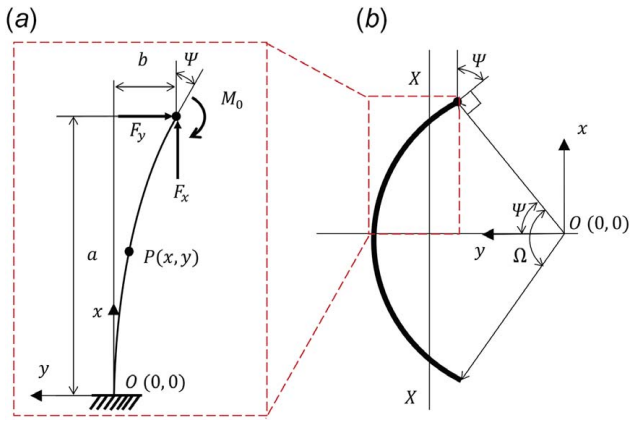

Fig. 7 (*a*) The cantilever beam model and (*b*) the deformed shape of the flexible beam

The Bernoulli–Euler equation is expressed as follows:

$$\frac{d\theta}{ds} = \frac{M(x, y)}{EI_z} \tag{14}$$

where I_z is the second moment of inertia in the z-axis direction and can be calculated by $I_z = Lt^3/12$. Equation (14) takes derivative to s we have

$$\frac{d^2\theta}{ds^2} = \frac{1}{EI_z}(-F_x \sin\theta(s) + F_y \cos\theta(s)) \tag{15}$$

Given the initial condition of $\theta(0) = 0$ and $\theta'(L) = M_0/EI_z$, we can calculate the lateral displacement of b and lateral deformation angle of Ψ. It is worth noting that Ψ is the tip deformation angle of half of the flexible beam, and the morphing angle of the entire flexible beam should be calculated as $\Omega = 2\Psi$.

Remember in this study, the purpose of the shape morphing is to change the second moment of inertia of I_{XX}, where $_{XX}$ is the centroid axis of the deformed flexible beam, as shown in Fig. 7(*b*). The location of the centroid axis can be expressed as $\bar{y} = \int_A y dA/A$, where A is the cross section of the flexible beam of $A = lt$. Then, the second moment of inertia of the deformed flexible beam can be calculated by $I_{XX} = \int_A \bar{y}^2 dA$.

In this study, only external forces (no external moments) are applied at the tip of the flexible beams. We can find the morphing angle Ω from Eq. (15) and the second moment of inertia I_{XX} for the flexible beam. Here, we consider a simple situation that the mapping from Ω to I_{XX} is bijective, and an Ω corresponds to a unique $I_{XX}(\Omega)$.

4.3 Lateral Stiffness of the Morphing Arm With the Classical Pseudo-Rigid-Body Model. The shape morphing arm is actually a compliant parallel-guiding mechanism. It can be modeled with a fixed-guided flexible segment as shown in Fig. 8(*a*). A classical fixed-guided PRB model is shown in Fig. 8(*b*). Consider a lateral force F applied at the stage, a resultant moment M_0 is generated to maintain the end of the flexible segment at a constant angle. The PRB model has a lateral displacement x and a deflection angle β. The link lengths of the PRB model are l_1, l_2, and l_3 and can be calculated by $l_1 = l_3 = (1 - \gamma)L/2$ and $l_2 = \gamma L$.

The four torsional springs of the fixed-guided PRB model are identical and the stiffness of each spring can be calculated by $k_{fg}(\Omega) = 2\gamma K_\theta EI_{xx}(\Omega)/L$. It is worth noting that in this article, the continuous stiffness variation is realized by morphing the shape of the flexible beam with an angle Ω, i.e., tuning the second moment of inertia $I_{xx}(\Omega)$.

The potential energy of the four torsional springs can be calculated by $V = 2k_{fg}(\Omega)\beta^2$. By virtual work principle, we have

$$F\delta x - \frac{dV}{d\beta}\delta\beta = 0 \tag{16}$$

Then, we can calculate the lateral force in terms of the deflection angle

$$F = \frac{4k_{fg}(\Omega)\beta}{\gamma L \cos\beta} \tag{17}$$

We further can calculate the lateral stiffness of the compliant arm

$$K_\delta(\Omega, \beta) = \frac{dF}{dx} = \frac{4}{\gamma^2 L^2} k_{fg}(\Omega) \frac{(\cos\beta + \beta\sin\beta)}{\cos^3\beta} \tag{18}$$

However, the original PRB model is not sufficiently accurate when compared with our later experimental results. The major problem is that the original PRB model assumes an ideal boundary condition, i.e., the flexible beams are rigidly fixed on both end houses. As a matter of fact, this assumption is not valid in this case. The middle part of the flexible beams (point D in Fig. 4) is rigidly fixed on the cable-driven mechanisms, while the bottom/up edges (point B_1' and B_2' in Fig. 4) are not fixed since they need to be morphed. In fact, the rigidity at B_1' and B_2' depends on the stall torque of the servo motor and the cable extensibility. That is to say, the boundary condition of the flexible beams is significantly affected by those factors. To improve the accuracy of the lateral stiffness model, we consider the compliance of the connection parts between the flexible beams and houses, and we model the compliance using four identical torsional springs.

4.4 An Improved Pseudo-Rigid-Body Model for the Lateral Stiffness of the Morphing Arm. In addition to the four torsional springs of the original PRB model, we model the compliance from the boundary condition with four identical torsional springs k_b, and the improved lateral stiffness model is shown in Fig. 8(*c*). Considering a lateral force of F, l_1, l_2, and l_3 deform with β_1, β_2, and β_3, respectively. The parameters of l_1, l_2, and l_3 of the optimized PRB model refer to those of the original PRB model. Note, $\beta_1 = \beta_3$ due to the assumption of symmetry. The lateral displacement can be calculated by $x = (1 - \gamma)L\sin\beta_1 + \gamma L\sin(\beta_1 + \beta_2)$. The lateral force in terms of the deformation angles can be calculated as follows:

$$F = 4k_b\beta_1 \frac{1}{(1 - \gamma)L\cos\beta_1 + \gamma L\cos(\beta_1 + \beta_2)} \tag{19}$$

$$F = \frac{4k_{fg}(\Omega)\beta_2}{\gamma L} \frac{1}{\cos(\beta_1 + \beta_2)} \tag{20}$$

Substituting Eq. (20) in Eq. (19) to eliminate the lateral force, we have the relationship of the deformation angles:

$$\frac{\beta_1}{\beta_2} = \frac{k_{fg}(\Omega)}{k_b}\left[\left(\frac{1 - \gamma}{\gamma}\right)\frac{\cos\beta_1}{\cos(\beta_1 + \beta_2)} + 1\right] \tag{21}$$

Given a specific lateral force F, we can always calculate the deformation angles β_1 and β_2 via any two equations from Eqs. (19)–(21). Then, one can find the lateral displacement of x. With the lateral force and the solved lateral displacement, the lateral stiffness of the compliant parallel-guiding mechanisms with fixture compliance can be obtained.

5 Experiment and Testing

5.1 The 3D-Printed Shape Morphing Arm. A robotic arm with tunable stiffness is fabricated by a 3D printer with acrylonitrile butadiene styrene (ABS) material, as shown in Fig. 9. The detailed cable-driven mechanism is shown in Figs. 9(*a*) and 9(*b*), and the bearing frames and universal transmission shafts are shown in

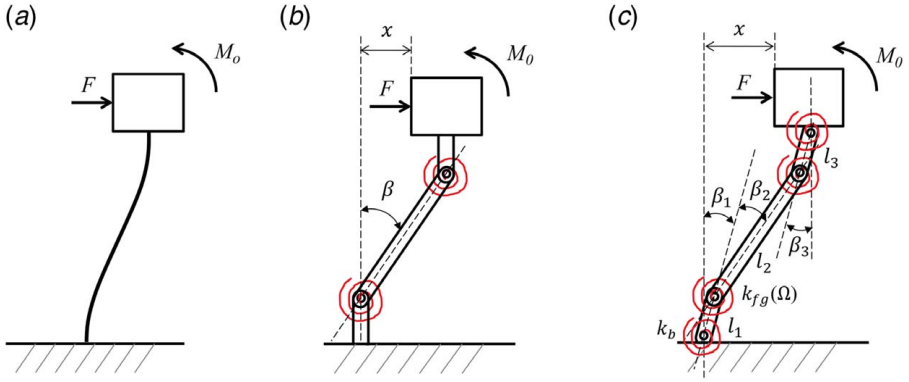

Fig. 8 (*a*) The fixed-guided flexible segment, (*b*) the corresponding PRB model, and (*c*) the improved PRB model

Fig. 9(*c*). The single morphing actuator is selected as HD 1235MG servo with a maximum torque of 3.954 Nm. The cable is selected as a coated stainless steel cable with a maximum force of 22.24 N. Eyebolts are used for the bending control pulleys and the base pulleys. Note the recovering pulleys may not be required since the flexible beam can provide a large recovery internal moment in the releasing period. We wind the cables based on the routes described in Sec. 3, and a single servo motor can continuously actuate the flexible beams from the flattened shape to curved shapes, and vice versa. The maximum motor angle is 130 deg, which corresponds to the maximum morphing angle of $\Omega = 90$ deg.

5.2 Lateral Stiffness Verification. We next test the variable lateral stiffness of the shape morphing arm. The static testing setup is shown in Fig. 10. The shape morphing arm is clamped at the base to the table. A force sensor (M5-100, 500×0.1 N) bears against the end house of the compliant arm and can be driven to travel along the screw of the Mark-10 system (ES30, 1000 N). The displacement is measured by a travel display (ESM001, 150×0.01 mm). A laptop is used to collect the data from the sensors. The NI controller (controller (NI cRIO-9014) is used to continuously control the morphing angle of the compliant robotic arm.

The servo motor is controlled from 0 deg to 130 deg with an increment of 10 deg. The lateral stiffness is calculated as the ratio of the lateral force over the lateral displacement. The experiment

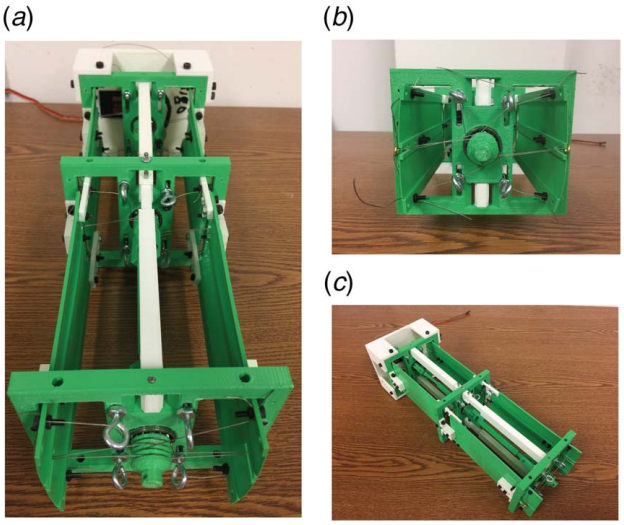

Fig. 9 The 3D-printed shape morphing arm with cable-driven mechanisms (the end house is detached to show the cable-driven mechanism)

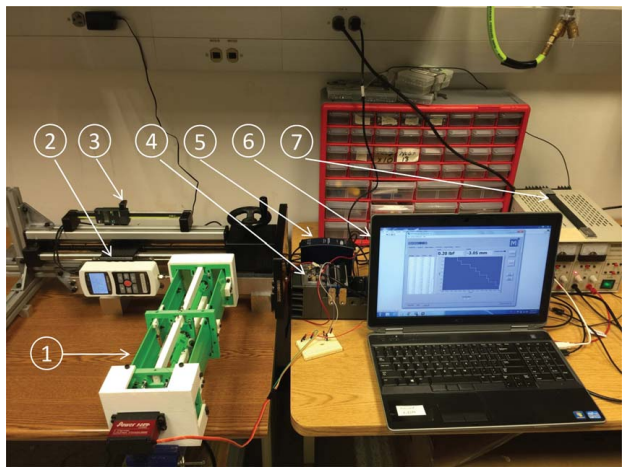

Fig. 10 The experiment setup for the static test: (1) the compliant robot arm, (2) the force sensor, (3) the travel display, (4) NI controller, (5) the power supply for NI controller, (6) laptop collecting data, and (7) The power supply for servo motor

results of the lateral stiffness versus the morphing angle are the "o" line, as shown in Fig. 11. The theoretical estimation of the lateral stiffness with the original PRB model and the improved lateral stiffness model are shown as the dashed line and solid line in Fig. 11, respectively. Noteworthy, E and k_b are determined

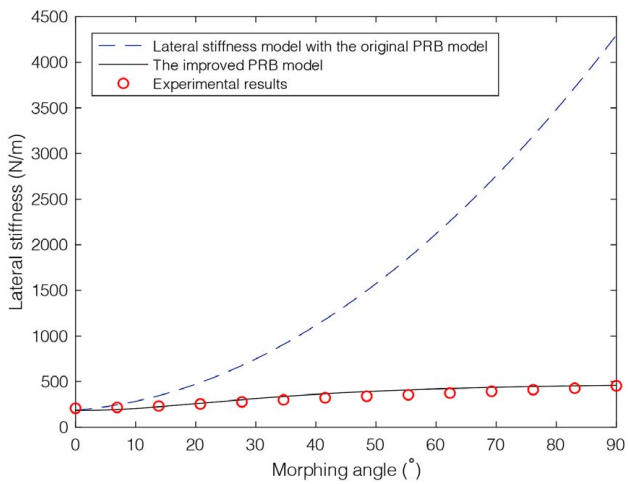

Fig. 11 Comparison of the original PRB model, the improved PRB model, and experimental testing results for lateral stiffness

from a set of separate experimental testing. It is identified that $E = 1.2$ Gpa and $k_b = 20$ N.m/rad give the minimal accumulated errors between the results from the improved model and the separate testing data. We then fixed these parameters for the improved model.

We found that the improved PRB model can well predict the experiment results, while the original PRB model deviates from the testing results. The experimental results show that a morphing angle from 0 deg to 90 deg can result in a lateral stiffness variation from 207 N/m to 458 N/m with a variety of 221.26%. In addition, the lateral stiffness with the PRB model also suggests that the lateral stiffness variation ratio of the shape morphing arm can be significantly improved if the boundary condition at the fixed end can be secured.

6 Discussions

The improved PRB model basically describes the following relationship: $K_\delta = f(E, L, l, t, \Omega, \beta_1, \beta_2)$, where K_δ represents the lateral stiffness of the variable stiffness link, and E, L, l, t are the design parameters representing the stiffness, Young's modulus, length, height, and thickness of the flexible beam. If a stiffness range is desired for a particular task, one may explore the range of the design parameters to achieve the target stiffness range according to the improved PRB model.

The modeling accuracy is significantly improved, comparing the improved PRB model with the original PRB model for the lateral stiffness of the robotic arm. However, the improved PRB model does not perfectly estimate the experiment results. There may be a few reasons resulting in the modeling errors. For instance, the flexible beams may not be ideally uniformly morphed although three sets of the cable-driven mechanism are used. The nonuniformly shape morphing can result in modeling errors. In addition, the transmission clearance and cable slackness may also introduce modeling errors. Last but not least, the 3D-printed ABS beam introduces the anisotropy material property, which may result in modeling errors as well.

It is worth mentioning that the PRB model (both the original and the improved one) only predicts the position of the end-effector, given a lateral force at the tip. It does not estimate the shape of the deformed beam. One may consider using other modeling methods if the shape of the link is critical for a particular task.

In this study, the idea of morphing shape is simple, but the realization of the actuation mechanisms is relatively complicated. The complex design is partially due to our goal of trying to minimize the number of actuators and morph the beam shape uniformly and symmetrically as well as to increase the moment arm to reduce required motor torque. The proposed variable stiffness link design is by no means to replace other variable stiffness solutions, such as the variable stiffness joints or actuators, but rather to provide an alternative solution or complementary solution to introduce mechanical compliance to the robotic system for safe physical human–robot interaction. Compared with other variable stiffness link designs in Refs. [41–43], which enable the robot link either rigid or compliant with switching mechanisms, this study developed an actively and continuously tunable stiffness arm with a relatively accurate lateral stiffness model.

The complex design results in challenges in practical manufacturing, such as maintaining cable tension as well as connecting the rigid and compliant components. There are four cable loops in each cable-driven system. In practice, it is important to adjust the tension of these cable loops, such that the shape morphing is symmetric. However, it is challenging to do so because it is difficult to precisely regulate the cable length by tying knots with cables. In addition, the cable length can be extended from the knots. We develop two methods to address this problem. First, the ends of the cable are actually not tied to the flexible beams. Instead, they are sandwiched between the screw nuts and the flexible beam as shown in Fig. 9. In this way, one can easily adjust the length (and tension) of the cable by releasing the pressure of the screw nuts. Second, we design sliding slots for the bending control pulleys to regulate the length (and tension) of the cable loops, as shown in Fig. 9(*b*). Here, we use eyebolts to serve as the bending control pulley. Both the position and orientation of the eyebolts can be adjusted to regulate the length and tension of the cable loops, and each cable loop can be adjusted independently.

Another notable challenge in practical manufacturing is the connection between the rigid and compliant components. There are three sets of the cable-driven mechanisms for the variable stiffness link. Each of the mechanisms has a rigid plate as shown in yellow part Fig. 3(*a*). These rigid plates are linked by the bearing frames and the universal transmission shafts. The central regions of the flexible beams (along the longitudinal direction) are fixed at the three rigid plates using screws and nuts. In practice, we want to avoid too thin connections between the flexible beams and the rigid plates because line contact may cause unstable situations. We also want to avoid too much surface contact for the connection because it will resist the beam's deformation. We address this problem by designing small surface contact structures, which are the blocks on top of the flexible beams as shown in Fig. 9(*c*). In this way, the centers of the flexible beams are firmly fastened to the rigid plate of the cable-driven mechanisms. Conversely, the sides of the flexible beams are tied with cables and can be pulled to deform by the cables.

A manipulator may be desired to have variable stiffness in any direction in space, which may require three orthogonal variable stiffnesses. In this study, the shape morphing arm is designed to allow the stiffness to be tunable only in its lateral direction, while the stiffness in other directions is not tunable and barely affected. For a robotics system or mechanical system requiring tunable stiffness in an arbitrary direction, the appropriate assembling of three arms in series may be one of the solutions.

7 Conclusion

This article presented a novel design of a tunable stiffness robot arm with cable-driven mechanisms for safe physical human–robot interaction. This study uses the PRB model for kinematics analysis of the actuation mechanisms and lateral stiffness modeling of the shape morphing arm. It is found that the classical PRB model may not accurately predict the statics of the compliant parallel-guiding mechanism if the boundary condition is not perfectly rigid. We introduced additional torsional springs into modeling, and the results show that the modeling accuracy is significantly improved. The testing results indicate that the lateral stiffness of the robot arm can achieve a variety of 221.26% given a morphing angle of 90 deg. The experiment demonstrated the feasibility of introducing mechanical compliance into robot links and the possibility of applying the variable stiffness link for safe physical human–robot interactions.

Acknowledgment

This material is based upon work supported by the National Science Foundation (Grant No. CMMI-1637656). Any opinions, findings, and conclusions or recommendations expressed in this material are those of the author(s) and do not necessarily reflect the views of the funding agencies.

Conflict of Interest

There are no conflicts of interest.

References

[1] Mutlu, B., and Forlizzi, J., 2008, "Robots in Organizations: The Role of Workflow, Social, and Environmental Factors in Human-Robot Interaction,"

Human-Robot Interaction (HRI), 2008 3rd ACM/IEEE International Conference on, Amsterdam, The Netherlands, Mar. 12–15, IEEE, pp. 287–294.
[2] Wolf, S., and Hirzinger, G., 2008, "A New Variable Stiffness Design: Matching Requirements of the Next Robot Generation," IEEE International Conference on Robotics and Automation, Pasadena, CA, May 19–23, pp. 1741–1746.
[3] Wolf, S., Eiberger, O., and Hirzinger, G., 2011, "The DLR FSJ: Energy Based Design of a Variable Stiffness Joint," 2011 IEEE International Conference on Robotics and Automation (ICRA), Shanghai, China, May 9–13, pp. 5082–5089.
[4] Friedl, W., Höppner, H., Petit, F., and Hirzinger, G., 2011, "Wrist and Forearm Rotation of the DLR Hand Arm System: Mechanical Design, Shape Analysis and Experimental Validation," 2011 IEEE/RSJ International Conference on Intelligent Robots and Systems, San Francisco, CA, Sept. 25–30, pp. 1836–1842.
[5] Ménard, T., Grioli, G., and Bicchi, A., 2014, "A Stiffness Estimator for Agonistic–Antagonistic Variable-Stiffness-Actuator Devices," IEEE Trans. Robot., **30**(5), pp. 1269–1278.
[6] Garabini, M., Passaglia, A., Belo, F., Salaris, P., and Bicchi, A., 2011, "Optimality Principles in Variable Stiffness Control: The VSA Hammer," 2011 IEEE/RSJ International Conference on Intelligent Robots and Systems, San Francisco, CA, Sept. 25–30, pp. 3770–3775.
[7] Schiavi, R., Grioli, G., Sen, S., and Bicchi, A., 2008, "VSA-II: A Novel Prototype of Variable Stiffness Actuator for Safe and Performing Robots Interacting With Humans," IEEE International Conference on Robotics and Automation, Pasadena, CA, May 19–23, pp. 2171–2176.
[8] Tonietti, G., Schiavi, R., and Bicchi, A., 2005, "Design and Control of a Variable Stiffness Actuator for Safe and Fast Physical Human/Robot Interaction," Proceedings of the 2005 IEEE International Conference on Robotics and Automation, Barcelona, Spain, Apr. 18–22, pp. 526–531.
[9] Zinn, M., Khatib, O., Roth, B., and Salisbury, J. K., 2004, "Playing It Safe [Human-Friendly Robots]," IEEE Robot. Automat. Mag, **11**(2), pp. 12–21.
[10] Migliore, S. A., Brown, E. A., and DeWeerth, S. P., 2005, "Biologically Inspired Joint Stiffness Control," Proceedings of the 2005 IEEE International Conference on Robotics and Automation, Barcelona, Spain, Apr. 18–22, pp. 4508–4513.
[11] Koganezawa, K., 2005, "Mechanical Stiffness Control for Antagonistically Driven Joints," 2005 IEEE/RSJ International Conference on Intelligent Robots and Systems, Edmonton, AB, Canada, Aug. 2–6, pp. 1544–1551.
[12] Pratt, G. A., and Williamson, M. M., 1995, "Series Elastic Actuators," 1995 IEEE/RSJ International Conference on Intelligent Robots and Systems 95, Proceedings on 'Human Robot Interaction and Cooperative Robots', Pittsburgh, PA, Aug. 5–9, pp. 399–406.
[13] She, Y., Meng, D., Cui, J., and Su, H.-J., 2017, "On the Impact Force of Human-Robot Interaction: Joint Compliance Vs. Link Compliance," 2017 IEEE International Conference on Robotics and Automation (ICRA), Singapore, May 29–June 3, pp. 6718–6723.
[14] She, Y., Song, S., Su, H.-J., and Wang, J., 2020, "A Comparative Study on the Effect of Mechanical Compliance for a Safe Physical Human–Robot Interaction," ASME J. Mech. Des., **142**(6), p. 063305.
[15] Park, J.-J., Kim, B.-S., Song, J.-B., and Kim, H.-S., 2008, "Safe Link Mechanism Based on Nonlinear Stiffness for Collision Safety," Mech. Mach. Theory., **43**(10), pp. 1332–1348.
[16] Zhang, M., Laliberté, T., and Gosselin, C., 2016, "Force Capabilities of Two-Degree-of-Freedom Serial Robots Equipped With Passive Isotropic Force Limiters," ASME J. Mech. Rob., **8**(5), p. 051002.
[17] López-Martínez, J., Blanco-Claraco, J. L., García-Vallejo, D., and Giménez-Fernández, A., 2015, "Design and Analysis of a Flexible Linkage for Robot Safe Operation in Collaborative Scenarios," Mech. Mach. Theory., **92**, pp. 1–16.
[18] She, Y., Su, H.-J., and Hurd, C. J., 2015, "Shape Optimization of 2d Compliant Links for Design of Inherently Safe Robots," ASME 2015 International Design Engineering Technical Conferences and Computers and Information in Engineering Conference, Boston, MA, Aug. 2–5, p. V05BT08A004.
[19] She, Y., Su, H.-J., Meng, D., Song, S., and Wang, J., 2018, "Design and Modeling of a Compliant Link for Inherently Safe Corobots," ASME J. Mech. Rob., **10**(1), p. 011001.
[20] Stilli, A., Wurdemann, H. A., and Althoefer, K., 2014, "Shrinkable, Stiffness-Controllable Soft Manipulator Based on a Bio-Inspired Antagonistic Actuation Principle," 2014 IEEE/RSJ International Conference on Intelligent Robots and Systems (IROS 2014), Chicago, IL, Sept. 14–18, pp. 2476–2481.
[21] Stilli, A., Wurdemann, H. A., and Althoefer, K., 2017, "A Novel Concept for Safe, Stiffness-Controllable Robot Links," Soft Robot., **4**(1), pp. 16–22.
[22] Gandarias, J. M., Wang, Y., Stilli, A., García-Cerezo, A. J., Gómez-de Gabriel, J. M., and Wurdemann, H. A., 2020, "Open-Loop Position Control in Collaborative, Modular Variable-Stiffness-Link (vsl) Robots," IEEE Robot. Automat. Lett., **5**(2), pp. 1772–1779.
[23] She, Y., Su, H.-J., Lai, C., and Meng, D., 2016, "Design and Prototype of a Tunable Stiffness Arm for Safe Human-Robot Interaction," ASME 2016 International Design Engineering Technical Conferences and Computers and Information in Engineering Conference, Charlotte, NC, Aug. 21–24, p. V05BT07A063.
[24] She, Y., Su, H.-J., Meng, D., and Lai, C., 2019, "Design and Modeling of a Continuously Tunable Stiffness Arm for Safe Physical Human-Robot Interaction," ASME J. Mech. Rob., **12**(1), p. 011006.
[25] She, Y., 2018, "Compliant Robotic Arms for Inherently Safe Physical Human-Robot Interaction," Ph.D. thesis, The Ohio State University, Columbus, OH.
[26] Zeng, X., Hurd, C., Su, H.-J., Song, S., and Wang, J., 2020, "A Parallel-Guided Compliant Mechanism With Variable Stiffness Based on Layer Jamming," Mech. Mach. Theory., **148**, p. 103791.
[27] Gao, Y., Huang, X., Mann, I. S., and Su, H.-J., 2020, "A Novel Variable Stiffness Compliant Robotic Gripper Based on Layer Jamming," ASME J. Mech. Rob., **12**(5), p. 051013.
[28] Frecker, M., Ananthasuresh, G., Nishiwaki, S., Kikuchi, N., and Kota, S., 1997, "Topological Synthesis of Compliant Mechanisms Using Multi-Criteria Optimization," ASME J. Mech. Des., **119**(2), pp. 238–245.
[29] Tolou, N., and Herder, J., 2009, "A Seminalytical Approach to Large Deflections in Compliant Beams Under Point Load," Math. Problems Eng., **2009**, pp. 1–13.
[30] Awtar, S., Slocum, A. H., and Sevincer, E., 2007, "Characteristics of Beam-Based Flexure Modules," ASME J. Mech. Des., **129**(6), pp. 625–639.
[31] Hopkins, J. B., and Culpepper, M. L., 2010, "Synthesis of Multi-Degree of Freedom, Parallel Flexure System Concepts Via Freedom and Constraint Topology (Fact)—Part I: Principles," Precis. Eng., **34**(2), pp. 259–270.
[32] Hopkins, J. B., and Culpepper, M. L., 2010, "Synthesis of Multi-Degree of Freedom, Parallel Flexure System Concepts Via Freedom and Constraint Topology (Fact). Part II: Practice," Precis. Eng., **34**(2), pp. 271–278.
[33] Morrison, T., and Su, H.-J., 2020, "Stiffness Modeling of a Variable Stiffness Compliant Link," Mech. Mach. Theory., **153**, p. 104021.
[34] Howell, L. L., and Midha, A., 1994, "A Method for the Design of Compliant Mechanisms With Small-Length Flexural Pivots," ASME J. Mech. Des., **116**(1), pp. 280–290.
[35] Howell, L. L., and Midha, A., 1995, "Parametric Deflection Approximations for End-Loaded, Large-Deflection Beams in Compliant Mechanisms," ASME J. Mech. Des., **117**(1), pp. 156–165.
[36] Song, S., She, Y., Wang, J., and Su, H.-J., 2020, "Toward Tradeoff Between Impact Force Reduction and Maximum Safe Speed: Dynamic Parameter Optimization of Variable Stiffness Robots," ASME J. Mech. Rob., **12**(5), p. 054503.
[37] Huang, C. L., Lin, W. Y., and Hsiao, K. M., 2010, "Free Vibration Analysis of Rotating Euler Beams at High Angular Velocity," Comput. Struct., **88**(17–18), pp. 991–1001.
[38] Derderian, J., Howell, L., Murphy, M., Lyon, S., and Pack, S., 1996, "Compliant Parallel-Guiding Mechanisms," Proceedings of the 1996 ASME Mechanisms Conference, Irvine, CA, Aug. 18–22, p. V02AT02A017.
[39] Culpepper, M. L., DiBiasio, C. M., Panas, R. M., Magleby, S., and Howell, L. L., 2006, "Simulation of a Carbon Nanotube-Based Compliant Parallel-Guiding Mechanism: A Nanomechanical Building Block," Appl. Phys. Lett., **89**(20), p. 203111.
[40] Howell, L. L., 2001, *Compliant Mechanisms*, John Wiley & Sons, Hoboken, NJ.
[41] Park, J.-J., Kim, B.-S., Song, J.-B., and Kim, H.-S., 2008, "Safe Link Mechanism Based on Nonlinear Stiffness for Collision Safety," Mech. Mach. Theory., **43**(10), pp. 1332–1348.
[42] López-Martínez, J., Blanco-Claraco, J. L., García-Vallejo, D., and Giménez-Fernández, A., 2015, "Design and Analysis of a Flexible Linkage for Robot Safe Operation in Collaborative Scenarios," Mech. Mach. Theory, **92**, pp. 1–16.
[43] Zhang, M., Laliberté, T., and Gosselin, C., 2016, "Force Capabilities of Two-Degree-of-Freedom Serial Robots Equipped With Passive Isotropic Force Limiters," ASME J. Mech. Rob., **8**(5), p. 051002.